

Testing Fundamental Physics with Distant Star Clusters: Analysis of Observational Data on Palomar 14^{*,**,***}

K. Jordi^{1,2}, E. K. Grebel², M. Hilker³, H. Baumgardt⁴, M. Frank², P. Kroupa⁴, H. Haghi^{4,5},
P. Côté⁶, and S. G. Djorgovski⁷

ABSTRACT

We use the distant outer halo globular cluster Palomar 14 as a test case for classical vs. modified Newtonian dynamics (MOND). Previous theoretical calculations have shown that the line-of-sight velocity dispersion predicted by these theories can differ by up to a factor of three for such sparse, remote clusters like Pal 14. We determine the line-of-sight velocity dispersion of Palomar 14 by measuring radial velocities of 17 red giant cluster members obtained using the Very Large Telescope (VLT) and Keck telescope. The systemic velocity of Palomar 14 is $(72.28 \pm 0.12) \text{ km s}^{-1}$. The derived velocity dispersion of $(0.38 \pm 0.12) \text{ km s}^{-1}$ of the 16 definite member stars is in agreement with the theoretical prediction for the classical Newtonian case according to Baumgardt et al. (2005). In order to exclude the possibility that a peculiar mass function might have influenced our measurements, we derived the cluster's main sequence mass function down to $0.53 M_{\odot}$ using archival images obtained with the Hubble Space Telescope. We found a mass function slope of $\alpha = 1.27 \pm 0.44$, which is, compared to the canonical mass function, a significantly shallower slope. The derived lower limit on the cluster's mass is higher than the theoretically predicted mass in case of MOND. Our data are consistent with a central density of $\rho_0 = 0.1 M_{\odot} \text{ pc}^{-3}$. We need no dark matter in Palomar 14. If the cluster is on a circular orbit, our spectroscopic and photometric results argue against MOND, unless this cluster experienced significant mass loss.

Subject headings: globular clusters: individual (Pal 14) – gravitation – stellar dynamics

^{*}Based on observations made with ESO Telescopes at the Paranal Observatories under programme ID 077.B-0769

^{**}Based on observations made with the NASA/ESA Hubble Space Telescope, obtained from the data archive at the Space Telescope Institute. STScI is operated by the association of Universities for Research in Astronomy, Inc. under the NASA contract NAS 5-26555.

^{***}Some of the data presented herein were obtained at the W.M. Keck Observatory, which is operated as a scientific partnership among the California Institute of Technology, the University of California and the National Aeronautics and Space Administration. The Observatory was made possible by the generous financial support of the W.M. Keck Foundation.

¹Astronomisches Institut, Universität Basel, Venusstrasse 7, CH-4102 Binningen, Switzerland

²Astronomisches Rechen-Institut, Zentrum für Astronomie der Universität Heidelberg, Mönchhofstrasse 12 - 14, D-69120 Heidelberg, Germany

³European Southern Observatory, Garching b.

1. Introduction

Is classical Newtonian dynamics valid on all scales? On Earth classical Newtonian dynamics describes all non-relativistic phenomena very well. With the exploration and study of the Universe, we can explore low acceleration regimes that can not be studied in our backyard and we observe deviations from the expected classical Newtonian

München, Germany

⁴Argelander Institut für Astronomie, Auf dem Hügel 71, D-53121 Bonn, Germany

⁵Institute for Advanced Studies in Basic Sciences (IASBS), P.O.Box 45195-1159, Zanjan, Iran

⁶Herzberg Institute of Astrophysics, National Research Council of Canada, Victoria, BC V9E 2E7, Canada

⁷Astronomy Department, California Institute of Technology, Pasadena, CA 91125, USA

behavior. E.g. the rotation curves of spiral galaxies do not show the classically expected Keplerian fall-off, but stay flat in the outer parts of these galaxies (Sofue & Rubin 2001). These flat rotation curves are commonly explained by introducing dark matter (DM). In the outer parts of the galaxies, DM is more abundant than regular baryonic matter and the gravitational effect of the DM on the baryons results in a flat rotation curve (Rubin et al. 1982). A major problem DM theory has encountered recently is the discovery that young tidal-dwarf galaxies also have rotation curves that imply a significant invisible matter component although they cannot be dominated by non-baryonic DM suggesting a non-classical physical solution (Gentile et al. 2007).

An alternative theory to DM is modified Newtonian dynamics (MOND; Milgrom 1983a,b; Bekenstein & Milgrom 1984). In MOND, the flat rotation curves of galaxies can be fitted without any assumption of unseen matter. According to MOND, Newtonian dynamics breaks down for accelerations lower than $a_0 \simeq 1 \times 10^{-8} \text{ cm s}^{-2}$ (Begeman et al. 1991; Sanders & McGaugh 2002). The acceleration \mathbf{a} in MONDian dynamics is given by the (heuristic) equation:

$$\mu\left(\frac{|\mathbf{a}|}{a_0}\right) \mathbf{a} = \mathbf{a}_N, \quad (1)$$

where $\mu(x)$ is an arbitrary function with the following limits:

$$\mu(x) = \begin{cases} x & \text{if } x \ll 1 \\ 1 & \text{if } x \gg 1. \end{cases} \quad (2)$$

Here, \mathbf{a}_N is the standard Newtonian acceleration and a_0 is the acceleration limit below which MOND is applicable.

It has been claimed that MOND has difficulties explaining the merging of galaxy clusters, where the baryonic matter is clearly separated from the gravitational mass, as found by gravitational lensing (Clowe et al. 2006). However, Angus et al. (2006, 2007) demonstrated that such systems are consistent with MOND, but do require the existence of some hot dark matter.

Baumgardt et al. (2005, BGK05) proposed to use distant, outer halo globular clusters (GCs) to distinguish between classical and modified Newtonian dynamics. They calculated the line-of-sight

velocity dispersion for 8 Galactic GCs in classical and in modified Newtonian dynamics. For these GCs the external acceleration due to the Milky Way and the internal acceleration due to the stars themselves are significantly below the critical limit of a_0 . The expected velocity dispersions in case of MOND exceed those expected in the classical Newtonian case by up to a factor of three (see Table 1 in BGK05).

Palomar 14 (Pal 14) is a diffuse GC in the outer halo of our Galaxy. Pal 14's sparseness, faintness, and large distance to the Sun makes it a difficult observational target, and therefore it did not receive much attention. The first radial velocity for a Pal 14 member star was measured by Hartwick & Sargent (1978) resulting in $81 \pm 3 \text{ km s}^{-1}$. Armandroff et al. (1992), based on radial velocity measurements for two stars, reported a systemic velocity of $72 \pm 3 \text{ km s}^{-1}$. The deepest ground-based color-magnitude diagram (CMD) of Pal 14 was published by Sarajedini (1997). He concluded that Pal 14 is 3-4 Gyr younger than halo GCs with a similar metallicity. Hilker (2006, H06) published photometric data on three GCs from the BGK05 sample: AM 1, Pal 3, and Pal 14. H06 confirmed Pal 14's youth of $\sim 10 \text{ Gyr}$. The data from his study are used here to obtain targets for our spectroscopic observations. Dotter et al. (2008) published a photometric study of Pal 14 based on archival data obtained with the Wide Field Planetary Camera 2 on board the Hubble Space Telescope. The authors confirm Pal 14's relative youth. Here the same data are used to obtain the cluster's mass function.

This paper is the second in a series that investigates theoretically and observationally the dynamics of distant star clusters. In the first paper (Haghi et al. 2009, HBK09), we derived theoretical models for pressure-supported stellar systems in general and made predictions for the outer-halo globular cluster Pal 14. In the current paper, we present a spectroscopic and photometric study of Pal 14, as a test case for the validity of MOND. I.e. we are measuring the velocity dispersion of Pal 14 in order to compare the measured value to the predicted values made for MOND and classical dynamics by HBK09. Further, we are determining the mass function of Pal 14 in order to infer the cluster's mass. The derived mass and velocity

dispersion are then compared to the predictions made by HBK09 for Pal 14 on a circular orbit in MOND.

The paper is organized as follows: In Section 2 we describe the observational material. In Sections 3 & 4 we present stellar radial velocities, the color-magnitude diagram and the mass function of Pal 14. In Section 5 we discuss the effects of our result for MOND and classical Newtonian gravity. The last Section concludes the paper with a summary.

2. Observations and Data Reduction

To distinguish between MOND and classical Newtonian dynamics we used two different kinds of observations. In order to measure Pal 14's velocity dispersion we obtained high-resolution spectra of red giant candidates towards Pal 14 with the Ultraviolet-Visual Echelle Spectrograph (UVES; Dekker et al. 2000) at the Very Large Telescope (VLT) of the European Southern Observatory (ESO) in Chile and with the High Resolution Echelle Spectrograph on the Keck I telescope. To be able to measure the cluster's mass function we used imaging data from the Hubble Space Telescope archive. In the following subsections we describe the reduction process of our observational data.

2.1. Spectroscopy with UVES

The photometry published by H06 shows the red giant branch and horizontal branch of Pal 14. Based on this photometry, we selected 16 of the 17 brightest red giants of Pal 14 for spectroscopy with UVES at the VLT. Our target stars cover the magnitude range $V = 17.3 - 19.6$ mag, which includes the brightest red giant of Pal 14 and goes down to the limit of faint stars observable with UVES. Figure 1 shows Pal 14's color-magnitude diagram. 15 of our targeted stars are probable red giants and one of the targets may be an AGB or evolved horizontal branch star. The significance of this different evolutionary state will be discussed in Section 3.1.

The spatial distribution of our spectroscopic targets is shown in Figure 2. The targeted stars lie mainly within two core radii with two stars in the cluster's outer region.

We used the Besançon Galaxy model (Robin et al.

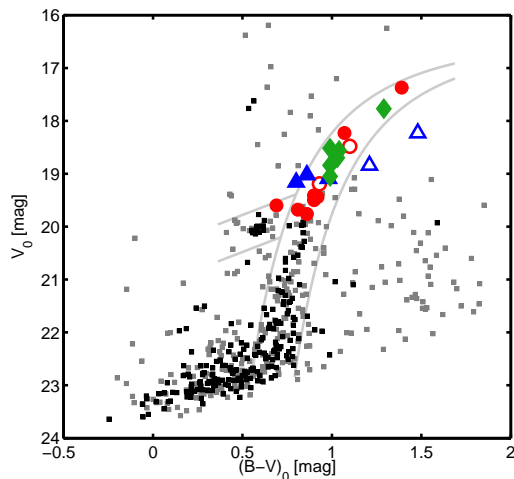


Fig. 1.— Color-magnitude diagram of Pal 14 from Hilker (2006). The observed targets for the radial velocity measurements with UVES are drawn as filled and open (red) circles. The open circles denote stars that were subsequently found to be the non-members (according to their radial velocity). The (blue) filled and open triangles are the stars observed with HIRES, the open triangles are the non-members. The (green) diamonds are the stars observed with UVES and HIRES. Dark grey dots are stars within 1 half light radius of Pal 14.

2003) to estimate the number of foreground stars in our sample. We extracted stars towards Pal 14 in an area on the sky covering $\sim 20r_h$, where $r_h = 1.28'$ is the half-light radius of Pal 14 (H06). The area covered with our sample stars is $\sim 2r_h$. We selected only those stars located in the gray curves shown in Figure 1 and having apparent magnitudes $V < 20$ mag, and colors $(B-V) > 0.65$ mag. The resulting number of foreground contaminants in the actual area covered predicted by the model is ~ 1 .

UVES was used in its RED 580nm setting covering the wavelength ranges 476 - 577 nm (in the lower chip) and 584 - 648 nm (in the upper chip). We divided the 16 target stars into three setups according to their brightness: the *bright* setup, containing the five brightest stars in the magnitude range $m_V = 17.37 - 18.52$, was observed for 4×60 min in total. The *medium* setup with the four next fainter stars ($m_V = 18.56 - 19.05$) was observed for 6×60 min in total. The *faint* setup, which included the seven least luminous stars ($m_V = 19.19 - 19.76$), was observed for 11×60 min in total. The observations were carried out in service mode within two observation periods, between May 30, 2006, and March 27, 2007. The pipeline reduced spectra ($R = 60\,000$) were used for the subsequent analysis.

The zero points in the reduced spectra were not identical. The sky emission lines in the single 1h-exposures were shifted with respect to each other. To correct for this we shifted the spectra to a common position of the sky emission lines. As a sky zero point location we used the sky lines in one of our own observed sky spectra, which we defined as reference spectrum. The resulting, shifted science exposures were further corrected for the heliocentric velocity shift. Finally all the shifted single 1h-exposure spectra were co-added for each star. In this way we get for the brightest star a $S/N = 16$ and for the faintest star $S/N = 4$.

2.2. Spectroscopy with HIRES

Within a program to study the internal kinematics of outer halo GCs (for details of the program see Côté et al. 2002) spectra for 11 candidate red giants in the direction of Pal 14 were obtained using the High Resolution Echelle Spectrograph (HIRES; Vogt et al. 1994) mounted on the Keck I telescope. The spectra, which were collected

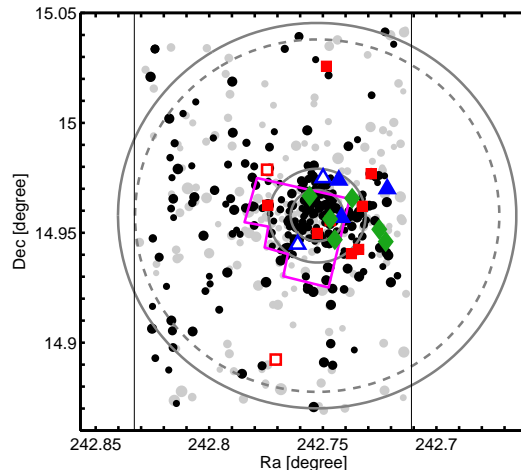


Fig. 2.— Spatial distribution of the spectroscopically observed Pal 14 stars. The observed targets for the radial velocity measurements with UVES are drawn as (red) filled and open circles. The two open squares mark the non-members (according to their radial velocity). The (blue) open and filled triangles are the stars observed with HIRES. The open triangles are the non-members. The (green) diamonds are the stars observed with UVES and HIRES. Dark grey dots are probable member stars according to their position in the CMD (see Figure 1). The grey concentric, solid circles are from inside out the core radius, the half-light radius and the tidal radius (H06); the dashed circle is the tidal radius calculated by BGK05. The (magenta) area is the HST/WFPC2 coverage.

during a single night in May 1998, have a resolution of $R = 45\,000$ (for the $0.866''$ entrance slit) and cover the wavelength range between 506 - 530 nm. The program stars were selected from CMDs published by Harris & van den Bergh (1984) and Holland & Harris (1992). The exposure times were adjusted on a star-to-star basis, varying between 900s and 2400s with a median value of 1800s. The spectra were reduced entirely within the IRAF¹ environment, in a manner identical to that described in Côté et al. (2002).

2.3. Radial velocity

To measure the radial velocity of our targeted stars we cross-correlated our final UVES and HIRES spectra with two high-resolution spectra of the UVES Paranal Observatory Project (UVES POP; Bagnulo et al. 2003): HD37811 (a G7 red giant) and HD45415 (a G9 red giant). The cross-correlation was done with the IRAF task *fxcor*. The heliocentric radial velocities of our two standard stars are: $v_{HD37811} = (-4.68 \pm 0.11) \text{ km s}^{-1}$, $v_{HD45415} = (52.70 \pm 0.04) \text{ km s}^{-1}$ (Melo 2007, private communication).

We determined the velocity shift of our sample stars relative to each of the two UVES POP stars. The UVES camera consists of two CCDs. For each pair of a UVES science target star and of a UVES POP star, we determined two radial velocities, one for the upper UVES chip and one for the lower UVES chip. These two velocities are averaged to a final velocity relative to the UVES POP star. Comparing the relative velocities measured for the two UVES POP stars, we find a mean difference of 0.1 km s^{-1} . Within the errors the two velocities are equal. The UVES science stars' radial velocity is the mean of the two velocities weighted by the Tonry-Davis R value (Tonry & Davis 1979) determined by *fxcor*.

For the HIRES sample, we determined the velocity of each science star relative to both UVES POP stars. Comparing the two relative velocities we find a mean difference of 0.07 km s^{-1} . The HIRES stars' radial velocity is the mean of these two measured velocities weighted by the Tonry-

Davis R value.

For 6 stars we have both UVES and HIRES spectra. To determine a common zero point of the two different samples we compared the measured velocities for these 6 stars. A mean velocity shift of $\Delta v = 0.64 \text{ km s}^{-1}$ was found. The shift is probably due to a different instrumental zero point. The final HIRES velocities are corrected for this shift. The shift can also be due to binarity or stellar variability. For two of the six stars we also have UVES measurements at two epochs, within the errors the velocities agree very well. Short-period binarity and variability can be excluded for these two stars. The error of the HIRES measurements for the five fainter stars is comparable to the mean shift. Five stars have a positive velocity shift and only one a negative. If all stars were binaries we would not expect a clear spread around a positive shift.

The final radial velocity for the 6 stars, with UVES and HIRES spectra, is the weighted mean of the measured velocities. For the remaining 15 stars we only have measurements of one instrument, therefore this velocity is taken as the final radial velocity of the star.

2.4. Photometry

We used imaging data obtained with the Hubble Space Telescope/Wide Field Planetary Camera 2 (HST/WFPC2) from the HST archive to obtain a deep CMD of Pal 14. The data were obtained as part of the proposal GO-6512 (PI: Hesser). The same data were used by Dotter et al. (2008). The WFPC2 images cover the entire area within the cluster's core radius (H06), about 67% of the area within the nominal half-light radius (H06), and only 7% of the area within the tidal radius (H06) (see Figure 2). The pipeline-reduced FITS files were run through multidrizle/tweakshifts (Koekemoer et al. 2002) to refine the image registration. All further processing was done on the original files together with the refined shifts, using the WFPC2 photometry package HSTphot (Dolphin 2000) and following the strategy outlined in the HSTphot User's Guide for preprocessing, photometry and artificial star tests. As in each subset of well aligned images in the same filter, the exposure times differed significantly, no co-adding was done. In Figure 1 we show the CMD of all stars brighter than

¹IRAF is distributed by the National Optical Astronomy Observatory, which is operated by the Association of Universities for Research in Astronomy, Inc., under cooperative agreement with the National Science Foundation.

28th mag detected by HSTphot with the following selections: the HSTphot sharpness parameter ($|sharpness| < 0.2$), HSTphot type parameter ($type < 3$, i.e. the star is either a single star or a possible unresolved binary), and magnitude errors $\sigma_{mag} < 0.2$ mag.

To determine the photometric errors we inserted artificial stars with known magnitudes. The deviations of the subsequently measured magnitudes to the inserted values let us determine the photometric errors shown in Figure 3.

2.5. Completeness

For a detailed analysis of the stars in Pal 14, we performed radius-dependent artificial star tests within HSTphot to determine the completeness of the observations. For the artificial star experiment we added $\sim 160\,000$ stars onto the image. For 7 annuli of a width of 0.3 arcmin we counted the number of artificial stars retrieved from the image with a magnitude not more than 0.2 mag different from the input value. In Figure 4 we show the seven completeness profiles (gray curves), which essentially fall on top of each other. Therefore, no radial dependence is observed, which is mainly due to the low density of Pal 14. The profile of the outermost annulus (solid line with squares) shows a decline at slightly brighter magnitudes. This is an artificial effect. The number of stars in this annulus is only 10% of the average number of stars in the other annuli. We used an averaged completeness profile in our analysis, shown as the black line. The 50% completeness limit is reached at $m_{555} = 27.21$ mag.

3. Spectroscopic Results

3.1. Individual stellar radial velocities

In Table 1, we list the measured heliocentric radial velocities ($v(UVES)$ and $v(HIRES)$) and their errors ($\sigma_{v(UVES)}$ and $\sigma_{v(HIRES)}$) for the 21 stars in our sample. The listed velocities v_{rad} are the weighted mean of the UVES and the HIRES observations. The listed errors are the propagated errors, weighted by the Tonry-Davis R value from the cross-correlations. Star 4, Star 10, HV051 and HV086 all have significantly different velocities than the majority of the measured stars which are centered around ~ 72.2 km s⁻¹: $v_{Star4} = (-32.14 \pm 0.16)$ km s⁻¹, $v_{Star10} = (50.44 \pm$

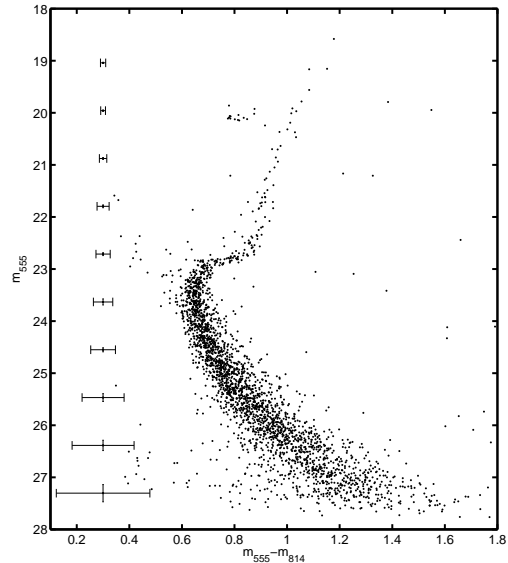


Fig. 3.— Color-magnitude diagram of Pal 14. We show the remaining stars after applying selections in the HSTphot parameters: sharpness, magnitude errors, and type. The CMD contains 2752 stars.

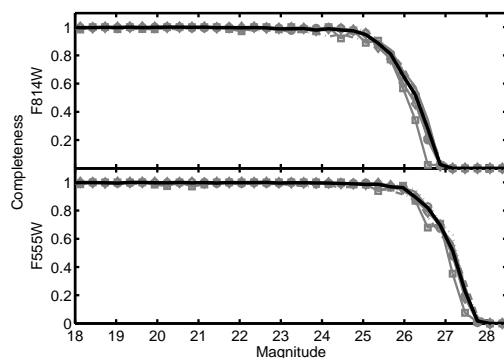


Fig. 4.— Completeness for the two filters F555W (lower plot) and F814W (upper plot). For each filter the completeness profile for seven annuli of width 0.3 arcmin are plotted as gray lines with different symbols, the black line is the overall completeness used in the data analysis.

TABLE 1
HELIOCENTRIC RADIAL VELOCITIES OF OUR SAMPLE STARS

Star ^a	Star ^b	$\alpha(2000)$ hh:mm:ss.ss	$\delta(2000)$ °:':"	m_V mag	$B - V$ mag	$v(UVES)$ km s ⁻¹	$\sigma_{v(UVES)}$ km s ⁻¹	$v(HIRES)$ km s ⁻¹	$\sigma_{v(HIRES)}$ km s ⁻¹	v_{rad} km s ⁻¹	$\sigma_{v_{rad}}$ km s ⁻¹	m?
1		16:11:05.81	14:57:45.1	17.37	1.39	72.53	0.07	72.53	0.07	Y
2	HV025	16:10:58.73	14:56:48.7	17.77	1.29	72.76	0.09	71.49	0.30	72.47	0.14	Y
3		16:10:54.90	14:58:36.7	18.23	1.07	71.75	0.14	71.75	0.14	Y
	HV051	16:10:59.98	14:58:30.1	18.23	1.48	-73.77	1.17	N
4		16:11:04.98	14:53:32.3	18.48	1.10	-32.14	0.16	N
5	HV007	16:10:59.24	14:57:22.5	18.52	0.99	71.68	0.18	73.23	0.53	72.21	0.30	Y
6	HH244	16:10:53.36	14:56:45.4	18.56	1.04	72.58	0.18	72.79	0.46	72.65	0.27	Y
7	HH201	16:10:54.04	14:57:05.6	18.70	1.03	72.62	0.18	72.68	0.49	72.64	0.27	Y
8	HV043	16:10:56.90	14:57:56.5	18.84	0.99	71.56	0.21	70.97	0.47	71.38	0.31	Y
	HV086	16:11:02.66	14:56:41.1	18.84	1.21	-155.31	0.85	N
	HV055	16:10:58.31	14:58:26.2	19.02	0.86	73.62	0.89	73.62	0.89	Y
9	HV104	16:11:01.40	14:57:60.0	19.05	0.99	73.49	0.21	73.53	0.91	73.50	0.43	Y
	HH042	16:10:53.20	14:58:12.0	19.09	0.98	71.94	0.35	71.94	0.35	Y
	HV004	16:10:58.03	14:57:25.1	19.16	0.80	73.23	0.56	73.23	0.56	Y
10		16:11:05.89	14:58:43.2	19.19	0.93	50.44	0.19	N
12	HV074	16:10:56.21	14:56:32.7	19.41	0.90	71.83	0.23	71.83	0.23	Y
13	HV075	16:10:56.98	14:56:25.8	19.44	0.92	72.33	0.41	72.33	0.41	Y
14	HV006	16:10:59.24	14:57:19.7	19.50	0.90	71.80	0.27	71.80	0.27	Y
15	HV042	16:10:55.84	14:57:43.4	19.60	0.69	69.99	0.38	69.99	0.38	Y?
16		16:10:59.62	15:01:32.9	19.68	0.81	72.14	0.43	72.14	0.43	Y
17	HV021	16:11:00.58	14:56:59.1	19.76	0.86	72.39	0.32	72.39	0.32	Y

^aIdentification from Hilker (2006)

^bIdentification from Harris & van den Bergh (1984) and Holland & Harris (1992)

0.18) km s⁻¹, $v_{HV051} = (-74.41 \pm 1.17)$ km s⁻¹ and $v_{HV086} = (-155.95 \pm 0.85)$ km s⁻¹. These four stars are categorized as non-members (open circles and triangles in Figures 1 & 2). The remaining 17 stars are considered to be members of Pal 14 (see last column in Table 1). The measured velocity of Star 15 is more than 3σ away from the mean of the other member stars. Therefore, we present all our results including and excluding Star 15.

3.2. The systemic velocity and the velocity dispersion

First, we determined the mean velocity and the global velocity dispersion for the two different measurement sets, respectively. We used the maximization method described in Pryor & Meylan (1993). The mean velocity for the HIRES measurements is (72.46 ± 0.29) km s⁻¹ and the velocity dispersion (0.66 ± 0.26) km s⁻¹. For the UVES measurements we find a mean velocity of (72.28 ± 0.15) km s⁻¹ and a velocity dispersion of (0.50 ± 0.11) km s⁻¹ if we exclude Star 15. Including Star 15, we find (72.12 ± 0.20) km s⁻¹ and (0.70 ± 0.15) km s⁻¹. The measurements of

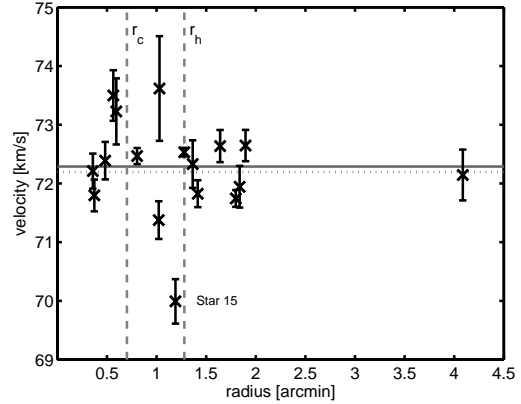


Fig. 5.— Radial distribution of stars with velocity measurements in Table 1. Black crosses indicate the 17 member stars of our sample of Pal 14. Star 15, for which the measured velocity is suspicious, is labeled. The horizontal solid line marks Pal 14's global radial velocity without Star 15, and the dotted line the radial velocity including Star 15. Further the core and half-light radii are indicated by dashed grey lines for an easier comparison with Figure 11.

TABLE 2
RADIAL VELOCITY AND VELOCITY DISPERSION OF PAL 14

Instrument	<i>velocity</i> <i>km s⁻¹</i>	<i>error_v</i> <i>km s⁻¹</i>	<i>dispersion</i> <i>km s⁻¹</i>	<i>error_d</i> <i>km s⁻¹</i>
UVES ^a	72.28 (72.12)	0.15 (0.20)	0.50 (0.70)	0.11 (0.15)
HIRES ^a	72.46	0.29	0.66	0.26
combined	72.28 (72.19)	0.12 (0.18)	0.38 (0.64)	0.12 (0.15)

^aThe first value is without the measurement of Star 15. The value in parentheses includes the measurement of Star 15.

the two samples agree very well.

Second, to determine the overall mean velocity and the global dispersion for all stars we also used the maximization method of Pryor & Meylan (1993). Including Star 15, we measured a mean heliocentric radial velocity for Pal 14 of $(72.19 \pm 0.18) \text{ km s}^{-1}$, excluding Star 15, $(72.28 \pm 0.12) \text{ km s}^{-1}$. Within the error bars the two values agree. Our results confirm the earlier measurements by Armandroff et al. (1992).

Figure 5 shows the radial profile of our measured velocities (Star 15 is labeled). The cluster’s mean velocity (for both cases) is marked by the solid (without Star 15) and dotted (with Star 15) horizontal line. In Table 2 we summarize the radial velocity and velocity dispersion measurements for the two instruments and for the combined stellar sample.

The global line-of-sight velocity dispersion for Pal 14 with Star 15 included is $(0.64 \pm 0.15) \text{ km s}^{-1}$ with 99% confidence limits of 0.41 km s^{-1} and 1.10 km s^{-1} . Without Star 15, the line-of-sight velocity dispersion is $(0.38 \pm 0.12) \text{ km s}^{-1}$ with 99% confidence limits of 0.26 km s^{-1} and 0.67 km s^{-1} . Within the errors the two values would agree. The theoretical prediction for the velocity dispersion of BGK05, for which a $M/L = 2$ was assumed, is $\sigma_{MOND} = 1.27 \text{ km s}^{-1}$ and $\sigma_{Newton} = 0.52 \text{ km s}^{-1}$. For both cases, when Star 15 is included or excluded, our results are more consistent with the classical Newtonian prediction, while the MONDian prediction is outside the 99% confidence limits.

As described above the measured velocity of Star 15 seems to be deviant. There are several possible explanations for this discrepant velocity of Star 15: *i*) Star 15 is a normal member of Pal 14. We performed a Monte Carlo simulation in order

to evaluate how likely the measured radial velocity profile is. In the Monte Carlo simulation we randomly drew velocities from a Gaussian distribution, which was newly initialized for each draw by calculating the mean velocity and standard deviation of our measured radial velocities randomly convolved with their errors. The radial distributions of all draws were added. We performed a KS-test of the simulated velocity distribution with the distribution of the actually measured velocity. The KS-test revealed a $< 1\%$ probability that the distribution that includes Star 15 comes from a Gaussian distribution, whereas the probability was $\sim 50\%$ that the distribution without Star 15 is Gaussian. This argues against Star 15’s membership in Pal 14. *ii*) Star 15 is not a red giant, but more likely an evolved horizontal branch (HB) star or an AGB star judging from its position in the CMD (see Figure 1). The used templates of a G7 (HD37811) and a G9 (HD45415) red giant may not be appropriate for Star 15. *iii*) Star 15 could be a binary. For our faint UVES sample (Stars 10-17) we have observations at two epochs: June, 2006 and March, 2007. Theoretically this allows us to measure a possible change in velocity due to binarity. The faintness and the therefore low S/N of Star 15’s spectra does not allow us to accurately measure the individual radial velocity for both epochs. The two measured velocities are $v_{2006} = (70.64 \pm 0.63) \text{ km s}^{-1}$ and $v_{2007} = (69.13 \pm 0.75) \text{ km s}^{-1}$. Within the errors the two velocities are the same. Nonetheless, this does not allow us to exclude long-period binarity. *iv*) A further cause for the large offset of Star 15’s velocity could be strong atmospheric variability, which can occur among AGB stars. However, from its position in the CMD, Star 15 would be an early-AGB star. In this

early phase, AGB stars are not yet pulsating very strongly (Habing & Olofsson 2003). With essentially only one observing epoch it is impossible to know about the star's variability. *v)* Another option might be that Star 15 is not a member of Pal 14. We computed a model velocity distribution of stars which are located within the light gray curves shown in Figure 1 using the Besançon Galaxy model (Robin et al. 2003) as described in Section 2.1. The expected velocity distribution, for stars with radial velocities $> -160 \text{ km s}^{-1}$, is shown in Figure 6. The number of stars in each bin is scaled to an area of $\sim 2r_h$, in order to reproduce the actually observed area. We expect about 9 stars to fulfill the photometric constraints. 0.5 stars have a radial velocity between 50 km s^{-1} and 75 km s^{-1} . Therefore, Star 15 could be a foreground contaminant.

4. Photometric results

In order to make predictions for the velocity dispersion in Newtonian and MONDian dynamics, we first have to determine the mass of Pal 14. The measured low velocity dispersion is in excellent agreement with the theoretical prediction of classical Newtonian dynamics, and a very strong indicator against MOND. The theoretical calculations by HBK09 show the dependence of velocity dispersion and mass (see Figure 8 in HBK09) for classical dynamics and MOND. For a given velocity dispersion the necessary mass is always smaller in MOND than in classical dynamics. Our derived low velocity dispersion is explainable in MOND if we find a low total mass for Pal 14. To constrain the mass in Pal 14, we analyzed Pal 14's CMD and main-sequence mass function.

4.1. Color-magnitude diagram

Figure 3 shows the HST CMD of Pal 14 with the remaining stars after the HSTphot parameter cuts (see Section 2.4 for details). The CMD reaches $\sim 4 \text{ mag}$ below the main-sequence turnoff, $m_{MSTO} = 23.63 \pm 0.01 \text{ mag}$, which allows us to theoretically determine the cluster's mass function down to $\sim 0.49 M_\odot$ (see Section 4.4). The CMD shows a well-populated main-sequence (MS), subgiant branch, red giant branch, red horizontal branch (HB), and some probable blue straggler stars. The presence of a red HB and its impli-

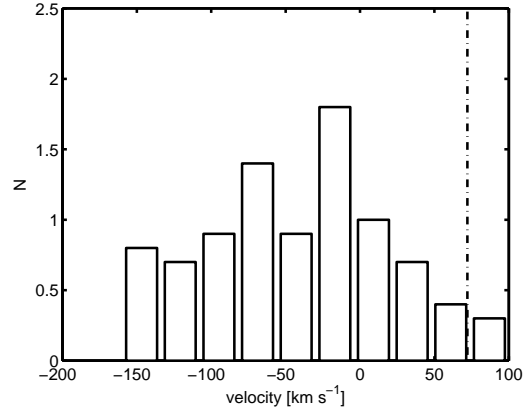


Fig. 6.— Expected velocity distribution based on the Besançon Galaxy model. Only stars that lie within the grey area in Figure 1 and that have a radial velocity larger than -160 km s^{-1} are counted (see text for more details). The dash-dotted, vertical line marks the systemic velocity of Pal 14, $\sim 72.2 \text{ km s}^{-1}$.

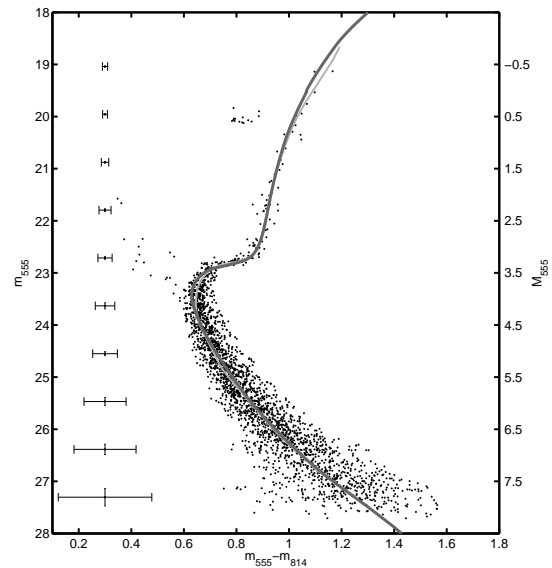


Fig. 7.— Color-magnitude diagram of our final sample of Pal 14 stars from WFPC2. The light gray line shows the derived cluster ridgeline, the dark gray line is the best fitted α -enhanced, $[\alpha/\text{Fe}]=+0.2$, Dartmouth isochrone with an age of 11.5 Gyr, $E(m_{555}-m_{814}) = 0.063$, and $(m - M)_{555} = 19.45 \text{ mag}$.

cations were discussed in Sarajedini (1997) and Dotter et al. (2008). As expected there is only little field star contamination of Milky Way stars due to the moderately high Galactic latitude of Pal 14 and due to the small field of view of WFPC2. Judging from the TRILEGAL Galaxy Model (Girardi et al. 2005), the number of contaminating foreground stars on our WFPC2 image in the CMD-area covered by Pal 14 is ~ 2 . The width of the main-sequence which we observe is due to a combination of the photometric errors and binary stars.

For our further analysis of Pal 14, we applied a stricter selection of our stellar sample. We determined the cluster’s fiducial ridgeline (see Figure 7, the light gray line). The ridgeline reproduces the mean location of the stellar distribution in the CMD. To derive the cluster’s ridgeline we adopted the method described in Glatt et al. (2008a). We selected all stars within 2σ of the ridgeline and added the blue stragglers and the HB stars for our final sample. The 2500 stars in our final sample are plotted in Figure 7.

4.2. Age & Distance

Pal 14 is known to be younger than typical halo GCs (Sarajedini 1997; Hilker 2006; Dotter et al. 2008) at its metallicity. We derived Pal 14’s age via isochrone fitting. We used the Dartmouth isochrones (Dotter et al. 2007), which have been shown to reproduce the location of the MS, subgiant branch, and red giant branch very well (Glatt et al. 2008b). We adopted the published spectroscopically determined metallicity of $[\text{Fe}/\text{H}] = -1.50$ (Harris 1996). Distance and reddening were treated as free parameters. A large number of isochrones was fitted using different combinations of age, distance, and reddening. We selected by trial-and-error the isochrone that best matched the above derived ridgeline.

With an α -enhanced isochrone, $[\alpha/\text{Fe}] = +0.2$, our best fit yields an age of (11.5 ± 0.5) Gyr, a reddening of $E(m_{555} - m_{814}) = 0.063$ (corresponding to $E(\text{B}-\text{V}) = E(m_{555} - m_{814})/1.2 = 0.05$ (Holtzman et al. 1995)), and an extinction corrected distance modulus of $(m - M)_{555,0} = 19.25$ mag. Sarajedini (1997) stated the age of Pal 14 is 3-4 Gyr younger than the age of similar halo GCs, H06 derived an age of 10 Gyr and Dotter et al. (2008) determined an age of 10.5 Gyr via α -

enhanced isochrone fitting. An α -enhancement is found for many of the Milky Way GCs (see, e.g. Carney 1996). Our new age determination reduces the offset to other halo GCs slightly.

From our CMD and the isochrone fit, we find a dereddened distance to Pal 14 of (71 ± 1.3) kpc, which places Pal 14 a bit closer to the Sun than previously thought. In comparison, H06 derived a distance to Pal 14 of 74.7 kpc. Dotter et al. (2008) derived an even larger distance of 79 kpc.

4.3. Luminosity function

The cluster’s MS luminosity function was derived by counting the number of stars, fainter than the MS turnoff at $m_{MSTO,0} = 23.44 \pm 0.01$ mag, in 0.5 mag wide bins separated by 0.1 mag along the dereddened m_{555} axis.

Furthermore, the WFPC2 images do not cover the entire projected spatial extension of the cluster on the sky. Our data cover the entire area within the cluster’s core radius (H06), about 67% of the area within the nominal half-light radius (H06), and only 7% of the area within the tidal radius (H06). The correction for the missing coverage within the half-light radius was done as follows. We derived the luminosity function for the stars within the annulus between the half-light and the core radius (n_{annulus}). We then corrected each magnitude bin of the entire distribution proportionally to the distribution of stars within the covered annulus:

$$N_{\text{area}} = N_{\text{obs}} + n_{\text{annulus}} \left(\frac{A_{\text{annulus}}}{A_{\text{covered}}} - 1 \right), \quad (3)$$

where A_{covered} is the area of the annulus covered by the WFPC2 image, and A_{annulus} the area of the annulus itself. The final correction was done for the photometric incompleteness (see Figure 4 and Section 2.5). We did not correct for potential foreground contaminants. The TRILEGAL Galaxy model only predicts a very small number of stars on our main-sequence. In Figure 8 we show the resulting luminosity function of Pal 14. The solid line shows the final number of stars per 0.5 mag bin. The errors are given as $N^{1/2}$.

Dotter et al. (2008) report an unusual flat luminosity function for Pal 14 between $V = 23$ mag and 28 mag. Their data was not corrected for incompleteness. Our MS luminosity function shows the

same flat behavior, correcting for incompleteness does not change the slope dramatically.

4.4. Mass function

The function $dN/dm \propto m^{-\alpha}$ describes the number of stars in the mass interval $[m, m + dm]$. We obtained such a mass function for Pal 14's MS. The upper boundary of the MS is at the turnoff, $m_{MSTO,0} = 23.44 \pm 0.01$ mag. Using the masses given by the 11.5 Gyr isochrone by Dotter et al. (2007), we have stellar masses on the MS covered by our photometry between $0.49 M_{\odot}$ and $0.79 M_{\odot}$. We binned the masses linearly into 10 bins of equal width of $0.03 M_{\odot}$. In Table 3, we list the center of the mass bins in the first column, and the number of observed stars (N_{obs}) for each bin in the second column.

We corrected the number of stars per mass bin for the same effects as in the case for the luminosity function. First, the observed number of stars per mass bin was corrected for the missing area coverage in the same way as described above (Table 3, column 3). Second, the mean of the stars' incompleteness was used as a correction factor. The corrected number of stars per mass bin is listed in Table 3, column 4. To fit a slope to our data we only considered data with a completeness factor > 0.50 (see last column in Table 3). This restriction leads to a MS mass function covering the range from $0.525 M_{\odot}$ to $0.79 M_{\odot}$. We fitted a slope to our data points in $\log(\text{number})$ vs $\log(\text{mass})$ space. In Figure 9 we plot the resulting mass function and the fitted slope of $\alpha = 1.27 \pm 0.44$ as the gray line. Dotter et al. (2008) find a similar mass function slope of $\alpha \approx 1.2$. The canonical Kroupa IMF (Kroupa 2001) in this notation is 2.35 for the given mass range. In Figure 9, the observed mass function is shown as the dash-dotted line. The dotted line is the mass function after the area corrections. The solid line denotes the completeness corrected number of stars.

Compared to the canonical slope of 2.35 Pal 14's mass function is flatter in the given mass range. De Marchi et al. (2007) compiled the mass function slope in the stellar mass range 0.3 to $0.8 M_{\odot}$ for 20 Galactic GCs of different sizes, concentrations, positions in the Galaxy, etc. Pal 14 has a (measured) concentration of $c = 0.85$ (H06). Clusters with a similar concentration span a mass

function slope range of $\alpha = -0.9 \dots 1.3$ (see Figure 1 in De Marchi et al. (2007)). The derived slope is comparable with the slope of similar clusters. E.g., NGC6809 has a concentration of 0.76 and a mass function slope of 1.3. This slope was derived around the cluster's half-light radius, where the impact of mass segregation is negligible (Paresce & De Marchi 2000). For Pal 14 we see an increasing number of stars per unit mass down to $0.525 M_{\odot}$. A sudden decrease below this low-mass limit would be a unique case as no Galactic GC is known to show an initial rise followed by a decrease.

In principle there are two reasons for such a depleted mass function: Either Pal 14 did form with only few low-mass stars, or the cluster is mass segregated and lost most of its low-mass stars through interaction with the Galactic tidal field. The small area covered by the WFPC2 image does not allow us to estimate the amount of mass segregation. In an upcoming paper we will discuss the issue of mass segregation in Pal 14 based on imaging data we obtained at the VLT.

4.5. Total mass & mass-to-light ratio

To estimate the mass of Pal 14 we corrected for the missing area within the half-light radius. We measured an observed mass for Pal 14's main-sequence $\mathcal{M}_{ms,obs} = (1\,340 \pm 50) M_{\odot}$ (above the 50% completeness limit). The errors are propagated from the measured photometry. Taking into account the stars brighter than the MS turn off, correcting for the missing area within the half-light radius and the completeness we get $\mathcal{M}_{cor} = (2\,200 \pm 90) M_{\odot}$ within the mass range $0.525 M_{\odot}$ to $0.83 M_{\odot}$. If we extrapolate by assuming that the measured slope of $\alpha = 1.27$ holds down to $0.5 M_{\odot}$ and assume a Kroupa-like mass function, $\alpha = 1.3$ for masses between $0.1 M_{\odot}$ and $0.5 M_{\odot}$, we have a total mass within the half-light radius for Pal 14 of $\mathcal{M}_{tot,hl} = (6\,020 \pm 500) M_{\odot}$.

The slope of the mass function for stars with masses $< 0.5 M_{\odot}$ is still under debate (Kroupa 2002; Elmegreen 2008). Pal 14 is very far from the Milky Way. It may have an eccentric orbit that would bring it much closer to the Milky Way at perigalacticon possibly leading to strong tidal interaction and to an enhanced loss of very low-mass stars. Richer et al. (2004, 2008) studied the main-sequence mass function of the GCs

TABLE 3
MASS FUNCTION OF PAL 14

Bin center \mathcal{M}_{\odot}	N_{obs}	$N_{corrected}$	N_f	σ_{N_f}	Completeness
0.51	114	152	706	59	0.21
0.54	249	330	542	30	0.61
0.57	196	255	316	20	0.81
0.60	258	328	372	21	0.91
0.63	201	274	282	17	0.97
0.66	226	306	311	18	0.98
0.69	219	282	286	17	0.99
0.72	212	271	273	17	0.99
0.75	213	268	270	17	0.99
0.78	225	301	302	18	1.00
0.81	289	366	367	20	1.00

NOTE.—Column 1 lists the center of our mass bins, column 2 the number of observed stars per bin, column 3 the number of stars per bin after correcting for the missing area coverage, column 4 contains the final number of stars per bin after correcting for completeness, column 6 lists the propagated error on the final number of stars per bin, and column 7 lists the average completeness value for the mass bin. (The numbers in columns 3, 4, and 5 are rounded to the nearest integer.)

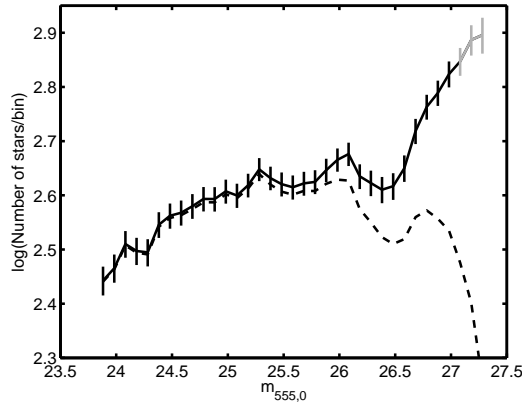


Fig. 8.— Luminosity function of Pal 14’s MS. The dashed line is the number of observed stars corrected for the missing area coverage. The solid line is the number of stars after the correction for photometric incompleteness (the grey dots mark points with a completeness $< 50\%$). The horizontal bars are the $N^{1/2}$ errors.

NGC 6397 and M 4 down to the hydrogen-burning limit. In the cluster cores they found mass function slopes of $\alpha = -0.7$, these cluster centers lack low-mass stars. Therefore, we also calculated the mass in Pal 14 for a mass function with a linearly declining slope for masses $< 0.5 M_{\odot}$ towards less massive stars ($\alpha = -1.0$). In that case the lower limit for the total mass within the half-light radius of Pal 14 is $\mathcal{M}_{tot,hl} = (2930 \pm 130) M_{\odot}$.

If we assume that light traces mass, then the half-light radius will also be the half-mass radius. Therefore we double the above numbers to estimate the total mass of Pal 14. The extrapolation with a Kroupa-like IMF for stellar masses between $0.1 M_{\odot}$ and $0.5 M_{\odot}$ yields a total mass of Pal 14 of $\mathcal{M}_{tot} \approx 12040 M_{\odot}$. With the declining mass function for masses $< 0.5 M_{\odot}$, we get a total mass of $\mathcal{M}_{tot} \approx 5860 M_{\odot}$. Considering stellar remnants will increase the mass further.

Using the total mass of Pal 14, we derive the mass-to-light ratio. The extrapolation with the Kroupa-like mass function yields $M/L = (2.2 \pm 0.4) M_{\odot}/L_{\odot}$. The extrapolation with the declining mass function gives $M/L = (1.1 \pm 0.1) M_{\odot}/L_{\odot}$.

5. Discussion

5.1. MOND?

In HBK09, we calculated the global line-of-sight velocity dispersion of isolated and non-isolated stellar systems in MOND for circular orbits. For details on the simulation see HBK09. In Figure 10, we plot the two curves from these calculations showing the global line-of-sight velocity dispersion as a function of stellar mass for the classical (open squares) and the modified Newtonian case (open circles). For a given total mass the velocity dispersion in the MONDian case is larger than in the classical theory. In our case, we observed a line-of-sight velocity dispersion (shown as the horizontal lines) and derived the cluster’s mass (shown as the vertical lines).

We measured a line-of-sight velocity dispersion of $(0.38 \pm 0.12) \text{ km s}^{-1}$, not including Star 15. For such a low dispersion, the theoretically predicted mass in MOND is $950^{+600}_{-400} M_{\odot}$, and in classical dynamics $8200^{+6000}_{-4000} M_{\odot}$. We have observed a lower limit of $(2200 \pm 90) M_{\odot}$ (marked in Figure 10 by the vertical line labeled *observed*) considering only the area within the half-light radius of Pal 14. Already the lower limit excludes the MONDian case, as we have observed more stellar mass than MOND predicts and the stars outside the cluster’s half-light radius are not considered yet. The total mass of $\sim 12500 M_{\odot}$ (in Figure 10 vertical line marked *extrapolated* ($\alpha = 1.3$)) is several times larger than the MONDian prediction. A declining extrapolation at the low-mass end down to $0.1 M_{\odot}$ gives a total mass of Pal 14 of $5860 M_{\odot}$ (in Figure 10 vertical line marked *extrapolated* ($\alpha = -1$)), which is also clearly higher than the MONDian prediction. The resulting dynamical mass-to-light ratio for the classical Newtonian case is $M/L_{dyn} = (1.48^{+1.00}_{-0.70}) M_{\odot}/L_{\odot}$.

If we include the measured velocity of Star 15, we find a line-of-sight velocity dispersion of $(0.64 \pm 0.15) \text{ km s}^{-1}$. According to the theoretical calculation of HBK09 the cluster mass in MOND would be $2600^{+1400}_{-1200} M_{\odot}$, and in classical dynamics $24000^{+11000}_{-10000} M_{\odot}$. In this case, the extrapolated mass is still larger than the predicted mass in MOND. Also, for the declining mass function for masses $< 0.5 M_{\odot}$ the total mass is larger than the MONDian prediction.

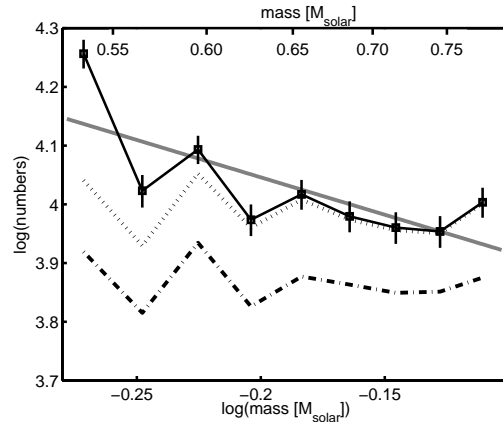


Fig. 9.— Mass function of Pal 14. The lowest (dash-dotted) line is the observed mass function for stars with masses between $0.49 M_{\odot}$ and $0.80 M_{\odot}$. The dotted line shows the mass function after correcting the number of stars per bin for the missing area coverage of the WFPC2 data. The top line also includes the correction for the photometric completeness. In gray the fitted slope $\alpha = 1.27 \pm 0.44$ is shown.

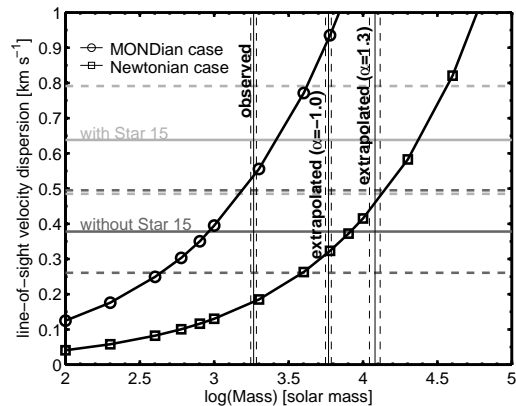


Fig. 10.— Theoretically predicted velocity dispersion as a function of mass. The two black curves are the predictions in MONDian dynamics (open circles) and in classical Newtonian dynamics (open squares). The observed velocity dispersions (and the errors) are drawn as the two horizontal lines, the light gray without Star 15, dark gray with Star 15. The vertical lines mark the observed lower mass limit and the two extrapolated lower mass limits.

Although the measured low velocity dispersion is an indication of whether MOND or classical Newtonian dynamics is correct, one can think of a scenario in which the cluster would be governed by MOND but shows at the same time a velocity dispersion consistent with the classically derived (low) value. In MOND the gravitational force is effectively stronger than in classical dynamics. The stars in a GC which resides in the MOND regime therefore acquire a higher internal velocity, thus leading to a shorter dynamical time and a faster relaxation time for the cluster (Ciotti & Binney 2004; Zhao 2005). Therefore, already after only a couple of orbits around the Galaxy, Pal 14 would have lost a large fraction of its low-mass stars and stellar remnants, leaving the cluster enriched in stars around the main-sequence turnoff and on the red giant branch. In one of Pal 14's perigalactica (if it is on an eccentric orbit), the cluster would become partially unbound and would expand, while it still resides in the classical Newtonian environment close to the Galaxy. The unbound cluster, then, would move further outward on its orbit and would eventually drift into the MONDian regime in the Galaxy's outskirts. As MOND is 'stickier' than classical Newtonian dynamics, the stars are bound more strongly again. As a consequence, an observer may measure a low velocity dispersion, similar to the value derived in classical dynamics. At the same time, the cluster's mass is small. For such a scenario to be valid, the cluster would have to be strongly effected by tidal forces, but should not move too far in to be completely destroyed. Detailed simulations on the influence of radial orbits on the velocity dispersion in MOND are necessary. Unfortunately no proper motion is available for Pal 14 in order to make any constraints on its orbit.

MOND is not the only modification of classical Newtonian dynamics. One other possible theory is modified gravity (MOG; Moffat 2005; Moffat & Toth 2008). MOG explains/predicts galaxy rotation curves, galaxy cluster masses, etc. and at the same time produces predictions consistent with classical dynamics for smaller systems, e.g. GCs. MOG predicts little or no observable deviation from classical Newtonian gravity for GCs with masses of a few times $10^6 M_\odot$ (Moffat & Toth 2008). Our result is consistent with the classical prediction and can, therefore,

neither support nor contradict MOG.

5.2. Velocity dispersion profile and dark matter

It is widely believed that globular clusters contain no dark matter (e.g., Moore 1996). Their dynamical masses closely match the values from population synthesis (McLaughlin & van der Marel 2005). The velocity dispersion profile of GCs should, therefore, show a Keplerian fall-off. Scarpa et al. (2007) studied velocity dispersion profiles of six GCs in the Galaxy. For the five high-concentration clusters in their study (ωCen , NGC 6171, NGC 6341, NGC 7078, NGC 7099) they found the predicted fall-off in the inner parts of the clusters, but also an unexpected flattening in the outer parts. On the other hand, for the low-concentration cluster NGC 288 they found a more or less flat dispersion profile. For the high-concentration clusters, the profiles always flatten at a radius where the acceleration is around the MONDian limit of a_0 for a mass-to-light ratio of 1. To draw any conclusion about MOND from this is rather difficult, as the discussed clusters' total accelerations are not below a_0 and therefore the effect of MOND is tiny or even not existent; the clusters are all too close to the Galactic center.

All our stars but one are located within $2.5'$ of the center of Pal 14. We derived the line-of-sight velocity dispersion profile with running radial bins, each bin containing six stars. Figure 11 shows the resulting velocity dispersion profile. Between $1'$ and $1.5'$ we derived the velocity dispersion either including Star 15 or excluding Star 15. The lower black squares are the case where Star 15 was not included, the upper gray squares the case including Star 15's velocity. For the case excluding Star 15, we can see (within the errors) a slightly declining velocity dispersion profile. The dashed curves in Figure 11 are the theoretically calculated profiles of HBK09. If we compare our dispersion profile to the theoretical predictions we see a slow fall-off towards outer radii for both. We have observed velocity measurements in the inner $2.5'$ (~ 50 pc ~ 3.6 core radii). On the other hand, Scarpa et al. (2007) showed the velocity dispersion profile of NGC 288, another sparse GC with a concentration of $c = 0.96$ (Harris 1996). They describe the profile to be flat out to 4.5 core radii. In order to improve the significance of the compar-

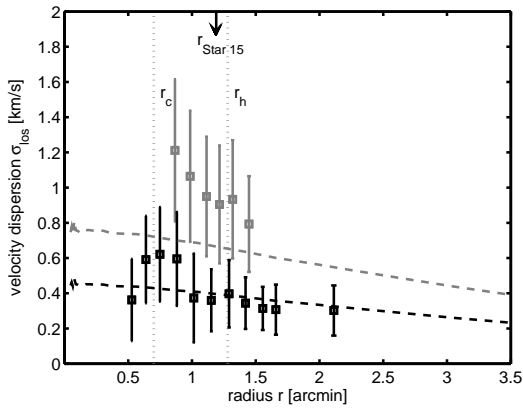


Fig. 11.— The velocity dispersion profile of Pal 14 using running bins with six stars in each bin. The black squares denote the velocity dispersion without Star 15. The gray squares denote these bins where Star 15 was included. The black and gray dashed curves are the theoretical dispersion profiles if Star 15 was included and excluded, respectively. The vertical, dotted lines are the core and half-light radii (H06), respectively. The arrow at the top of the plot marks the radial distance of Star 15 from the cluster center.

ison of the theoretical prediction and the observational data for Pal 14 as well as of the comparison with similar clusters, spectroscopic data out to larger radii are needed for Pal 14.

We treat this GC the same way as dwarf spheroidal (dSph) galaxies in Madau et al. (2008) to calculate the central density, using $\rho_0 = 166\eta\sigma^2/r_c^2 M_\odot pc^{-3}$, setting $\eta = 1$, $r_c = 0.7' = 14.5 pc$, and $\sigma = 0.38 \pm 0.12 km s^{-1}$. We find a central density of $\rho_0 = 0.1 \pm 0.07 M_\odot pc^{-3}$. A value which is very similar to values found for dSph galaxies (see e.g. Table 1 in Madau et al. (2008)). On the other hand, if we derive the density within the half-light radius from our mass estimate $\mathcal{M}_{tot,hl} = (6020 \pm 500) M_\odot$ and $r_h = 1.28' = 26 pc$, we find $\rho = 0.08 \pm 0.01 M_\odot pc^{-3}$. Within the errors the two values agree. We do not need to assume DM for Pal 14.

6. Summary

Modified Newtonian dynamics has proven to be quite successful on galactic and also on intergalactic scales (Sanders & McGaugh 2002). However, not only galaxy size objects must be correctly explained by MOND. Objects with similar low accelerations, for which there is no need for additional, unseen matter such as GCs must be described correctly by this modified theory, as well. Hence, we have studied the outer halo GC Pal 14 to test whether modified or classical Newtonian dynamics applies. Pal 14 has an internal and external acceleration that are both significantly smaller than a_0 . Also, the total acceleration of stars in Pal 14 is still significantly smaller than a_0 and therefore, Pal 14 is an excellent test object for the two theories.

We determined the radial velocities of 17 giant stars in Pal 14. Using the measurements of all 17 giants, we confirmed the cluster's mean radial velocity of $(72.19 \pm 0.18) km s^{-1}$ and measured a global line-of-sight velocity dispersion of $(0.64 \pm 0.15) km s^{-1}$ (see Section 3 for details). Excluding Star 15, we find a similar systemic velocity of Pal 14 of $(72.28 \pm 0.12) km s^{-1}$ and a lower velocity dispersion of $(0.38 \pm 0.12) km s^{-1}$. These velocity dispersions lead to dynamical masses of $950^{+600}_{-400} M_\odot$ in modified dynamics, and $8200^{+6000}_{-4000} M_\odot$ in classical dynamics for the case without Star 15. In the case including Star 15 we expect total masses of Pal 14 of $2600^{+1400}_{-1200} M_\odot$ in

MOND, and $24\,000^{+11\,000}_{-10\,000} M_{\odot}$ in classical dynamics.

The mass function of Pal 14 has a slope of $\alpha = 1.27 \pm 0.44$ in the mass range $0.53M_{\odot}$ to $0.78M_{\odot}$ and is thus flatter than the canonical mass function. This is consistent with the cluster being formed mass segregated with a normal (canonical) IMF but suffering major mass loss through gas expulsion (Marks et al. 2008). The HST image covers only 7% of the area within the cluster's tidal radius, but more than 2/3 of the area within the half-light radius. The observed total mass within the half-light radius with an extrapolation to lower masses with a Kroupa-like mass function is $\sim 6\,020 M_{\odot}$. If we extrapolate with a linearly declining slope for masses $< 0.5M_{\odot}$, we get a total mass within the half-light radius of $\sim 2\,930 M_{\odot}$. In both cases, these values are lower limits. By doubling the numbers to get a rough estimate of the total mass of Pal 14, we get numbers that are substantially higher than the predictions made by HBK09 for MOND. Hence, the cluster's current stellar content is an indication against MONDian dynamics, unless the cluster is on an eccentric orbit.

If Pal 14 is on a circular orbit, MOND cannot explain the low velocity dispersion and the measured mass simultaneously. If Pal 14 is on an eccentric orbit, the low velocity dispersion may still be a problem for MOND, but the measured mass function slope, being flatter than the canonical value, does not allow us to draw a definite conclusion. With the sample of BGK05 and the theoretical predictions of BGK05 and HBK09 we have a basis for extending the study to other outer halo, low-mass Galactic GCs to further refine and improve the tests of gravitational theory.

We like to thank Marina Rejkuba for her advice deriving the radial velocities, and Katharina Glatt for her help with the isochrone fitting and the age determination of Pal 14. KJ and EKG acknowledge support from the Swiss National Foundation through grant numbers 20020-122140 and 20020-113697. SGD acknowledges a partial support from the NSF grant AST-0407448

REFERENCES

- Angus, G. W., Famaey, B., & Zhao, H. S. 2006, *MNRAS*, 371, 138
- Angus, G. W., Shan, H. Y., Zhao, H. S., & Famaey, B. 2007, *ApJ*, 654, L13
- Armandroff, T. E., Da Costa, G. S., & Zinn, R. 1992, *AJ*, 104, 164
- Bagnulo, S., Jehin, E., Ledoux, C., Cabanac, R., Melo, C., Gilmozzi, R., & The ESO Paranal Science Operations Team 2003, *The Messenger*, 114, 10
- Baumgardt, H., Grebel, E. K., & Kroupa, P. 2005, *MNRAS*, 359, L1 [BGK05]
- Begeman, K. G., Broeils, A. H., & Sanders, R. H. 1991, *MNRAS*, 249, 523
- Bekenstein, J., & Milgrom, M. 1984, *ApJ*, 286, 7
- Carney, B. W. 1996, *PASP*, 108, 900
- Ciotti, L., & Binney, J. 2004, *MNRAS*, 351, 285
- Clowe, D., Bradač, M., Gonzalez, A. H., Markevitch, M., Randall, S. W., Jones, C., & Zaritsky, D. 2006, *ApJ*, 648, L109
- Côté, P., Djorgovski, S. G., Meylan, G., Castro, S., & McCarthy, J. K. 2002, *ApJ*, 574, 783
- Dekker, H., D'Odorico, S., Kaufer, A., Delabre, B., & Kotzlowski, H. 2000, *Proc. SPIE*, 4008, 534
- De Marchi, G., Paresce, F., & Pulone, L. 2007, *ApJ*, 656, L65
- Dolphin, A. E. 2000, *PASP*, 112, 1383
- Dotter, A., Chaboyer, B., Jevremović, D., Baron, E., Ferguson, J. W., Sarajedini, A., & Anderson, J. 2007, *AJ*, 134, 376
- Dotter, A., Sarajedini, A., & Yang, S.-C. 2008, *AJ*, 136, 1407
- Elmegreen, B. G. 2008, *ArXiv e-prints*, 803, arXiv:0803.3154, 397, 38
- Girardi, L., Groenewegen, M. A. T., Hatziminaoglou, E., & da Costa, L. 2005, *A&A*, 436, 895

- Gentile, G., Famaey, B., Combes, F., Kroupa, P., Zhao, H. S., & Tiret, O. 2007, *A&A*, 472, L25
- Glatt, K., et al. 2008, *AJ*, 135, 1106
- Glatt, K., et al. 2008, *AJ*, 136, 1703
- Habing, H. J., & Olofsson, H. 2003, Asymptotic giant branch stars, by Harm J. Habing and Hans Olofsson. *Astronomy and Astrophysics Library*, New York, Berlin: Springer, 2003,
- Haghi, H., Baumgardt, H., Kroupa, P., Grebel, E. K., Hilker, M., & Jordi, K. 2009, arXiv:0902.1846 [HBK09]
- Harris, W. E., & van den Bergh, S. 1984, *AJ*, 89, 1816
- Harris, W. E. 1996, *AJ*, 112, 1487
- Hartwick, F. D. A., & Sargent, W. L. W. 1978, *ApJ*, 221, 512
- Hilker, M. 2006, *A&A*, 448, 171 [H06]
- Holland, S., & Harris, W. E. 1992, *AJ*, 103, 131
- Holtzman, J. A., Burrows, C. J., Casertano, S., Hester, J. J., Trauger, J. T., Watson, A. M., & Worthey, G. 1995, *PASP*, 107, 1065
- Koekemoer, A. M., Fruchter, A. S., Hook, R. N., & Hack, W. 2002, *The 2002 HST Calibration Workshop : Hubble after the Installation of the ACS and the NICMOS Cooling System*, S. Arribas, A. Koekemoer, & B. Whitmore. Baltimore, MD: Space Telescope Science Institute, p.337
- Kroupa, P. 2001, *MNRAS*, 322, 231
- Kroupa, P. 2002, *Science*, 295, 82
- Madau, P., Diemand, J., & Kuhlen, M. 2008, *ApJ*, 679, 1260
- Marks, M., Kroupa, P., & Baumgardt, H. 2008, *MNRAS*, 386, 2047
- McLaughlin, D. E., & van der Marel, R. P. 2005, *ApJS*, 161, 304
- Milgrom, M. 1983, *ApJ*, 270, 365
- Milgrom, M. 1983, *ApJ*, 270, 371
- Moore, B. 1996, *ApJ*, 461, L13
- Moffat, J. W. 2005, *Journal of Cosmology and Astro-Particle Physics*, 5, 3
- Moffat, J. W., & Toth, V. T. 2008, *ApJ*, 680, 1158
- Aaronson, M., & Peterson, R. C. 1986, *ApJ*, 302, L45
- Paresce, F., & De Marchi, G. 2000, *ApJ*, 534, 870
- Pryor, C., & Meylan, G. 1993, *Structure and Dynamics of Globular Clusters*, 50, 357
- Richer, H. B., et al. 2004, *AJ*, 127, 2771
- Richer, H. B., et al. 2008, *AJ*, 135, 2141
- Robin, A. C., Reylé, C., Derrière, S., & Picaud, S. 2003, *A&A*, 409, 523
- Rubin, V. C., Thonnard, N. T., & Ford, W. K., Jr. 1982, *AJ*, 87, 477
- Sanders, R. H., & McGaugh, S. S. 2002, *ARA&A*, 40, 263
- Sarajedini, A. 1997, *AJ*, 113, 682
- Scarpa, R., Marconi, G., Gilmozzi, R., & Carraro, G. 2007, *The Messenger*, 128, 41
- Sofue, Y., & Rubin, V. 2001, *ARA&A*, 39, 137
- Tonry, J., & Davis, M. 1979, *AJ*, 84, 1511
- Vogt, S. S., et al. 1994, *Proc. SPIE*, 2198, 362
- Zhao, H. 2005, arXiv:astro-ph/0508635